Solid barriers for windblown sand mitigation: Aerodynamic behavior and conceptual design guidelines

Solid barriers for windblown sand mitigation: aerodynamic behavior and conceptual design guidelines

Luca Bruno[a,d,*], Davide Fransos[b,d], Andrea Lo Giudice[b,c,d]

[a] *Politecnico di Torino, Department of Architecture and Design, Viale Mattioli 39, I-10125, Torino, Italy*
[b] *Optiflow Company, 160, Chemin de la Madrague-Ville, F-13015, Marseille, France*
[c] *Politecnico di Torino, Department of Mathematical Sciences"Giuseppe Luigi Lagrange", Corso Duca degli Abruzzi, 24, I-10129, Torino, Italy*
[d] *Windblown Sand Modeling and Mitigation joint research group*

Abstract

Protection from windblown-sand is one of the key engineering issues for construction and maintenance of human infrastructures in arid environments. In the last century, several barriers with different shapes have been proposed in order to overcome this problem, but literature lacks of a systematic performance quantitative analysis, and the key geometric parameters that promote sedimentation have not been yet recognized. A deep understanding of the aerodynamics effects of sand barrier on the flow is an unavoidable step to achieve these objectives. The present computational study aims to comparatively analyze different kinds of windblown sand mitigation solid barriers, clarify their working principles, extract from the aerodynamics analysis key geometrical features of the barriers and relate them to the sand trapping performances. Approximated metrics for performance assessment are introduced using aerodynamic parameters. The performances of an innovative solid barrier and the ones of commonly used solid barriers are compared in terms of these metrics. The effects of incoming wind velocity profiles on sand trapping performances are evaluated as well. An empirical dimensionless performance estimator is proposed and used to provide general design guidelines.

Keywords: windblown sand, mitigation measures, solid barrier, trapping efficiency, design guidelines, Computational Wind Engineering

1. Introduction

The engineering interest about windblown sand is dictated by the harmful interactions that sand can have with a number of human infrastructures in

*Corresponding author
Email address: luca.bruno@polito.it (Luca Bruno)
URL: http://www.polito.it/wsmm (Luca Bruno)

arid environments (Middleton and Sternberg, 2013), such as pipelines (Kerr and Nigra, 1952) and industrial facilities (Alghamdi and Al-Kahtani, 2005), farms (Stigter et al., 2002), towns (Zhang et al., 2007) or single buildings (Bofah et al., 1991), roads (Redding and Lord, 1981) and railways. In particular, the wind-induced accumulation of sand poses key challenges for railways crossing deserts and arid regions (e.g. Zhang et al., 1995, 2010; Zakeri and Forghani, 2012; Cheng and Xue, 2014; Cheng et al., 2015).

Strategies to overcome the problem usually go under the name of Sand Mitigation (SM). Most of SMs are intended to interrupt the sand transport process and to promote its sedimentation away from human infrastructures to be protected. The devices built to put in place this strategy (Sand Mitigation Measures, SMMs) are located along the windblown sand path upwind the infrastructure to be protected (Figure 1). Such devices range from stabilized sand

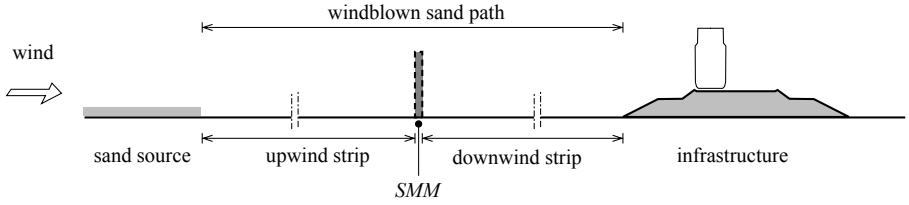

Figure 1: Conceptual scheme of the sand source, SMM and infrastructure: cross section.

berms and ditches to porous fences and solid barriers, or different combinations of them.

Porous fences have been widely investigated in the scientific literature since the early studies at the beginning of the 20th century. The research activity about fences has been recently reviewed with respect to both wind loads (Giannoulis et al., 2012), aerodynamics (Hong et al., 2015), and induced morphodynamics (Li and Sherman, 2015). Very briefly, the porosity ratio and its distribution is commonly considered the most important single parameter driving the design and controlling the performance of a sand fence of a given height, and for a given incoming wind.

Conversely, to our best knowledge, scientific studies on the aerodynamics and morphodynamics of windblown sand solid barriers, i.e. having null porosity, are surprisingly scarce.

The aerodynamics of a solid straight vertical wall has been investigated by Baines (1963), Good and Joubert (1968) and Letchford and Holmes (1994) with wind tunnel tests in nominal 2D conditions. In particular, Baines (1963) shows that the local wind pattern around it is characterized by a large reversed flow region in the wake of the barrier and by a stable clockwise eddy with horizontal axis along the upwind front of the wall below the stagnation point (Fig. 2-a). This upwind eddy is the distinctive flow structure with respect to the flow pattern around a porous fence (e.g. Dong et al., 2007, - Figure 4), the latter depending on porosity value. In particular, from medium to high porosity, it is characterized by the absence of the stagnation point and by the sole reversed

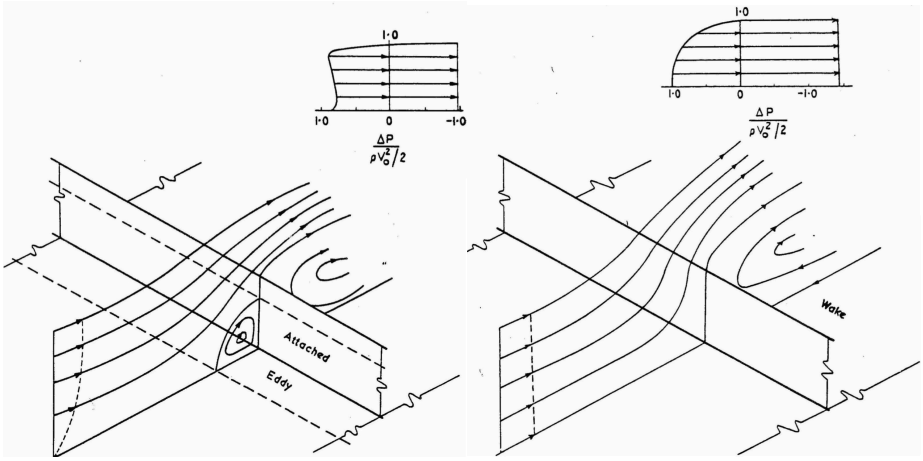

(a) (b)

Figure 2: Flow patterns around a solid straight vertical wall: log-type (a) and constant (b) incoming velocity profile (Reprinted from Baines, 1963)

region in the wake. According to Baines (1963), the upwind eddy results from the curvature of the incoming velocity profile, while it vanishes for a constant incoming wind field (Fig. 2-b).

In a morphodynamic perspective, solid barriers are usually adopted as a limit term of reference in the performance assessment of fences having various porosity ratios and distribution, e.g. Cornelis and Gabriels (2005). On one hand, it is widely accepted that fences with an optimal porosity of around 40-50% (e.g. Savage and Woodhouse, 1968; Bofah and Al-Hinai, 1986) have a sand trapping efficiency (defined as the maximum volume of accumulated sand per fence unit length) higher than a solid barrier. On the other hand, the distribution of the accumulated sand around porous fences and solid barrier is qualitatively different. Hotta and Horikawa (1991) show that sand mainly accumulates in the upwind strip of a solid straight vertical wall, while porous fences involve sedimentation on both strips, and have more sand deposited in the downwind one (Fig. 3).

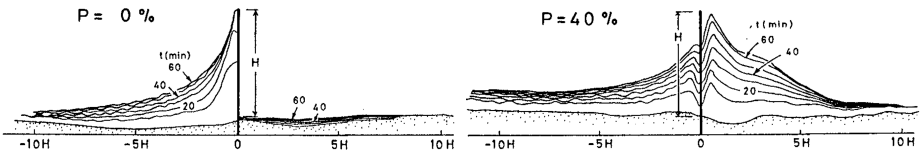

(a) (b)

Figure 3: Distribution of the accumulated sand around a solid straight vertical wall (a) and a fence with porosity 40% (b) (Reprinted from Hotta and Horikawa, 1991, Copyright 1990, with permission to reuse under a Creative Commons Attribution License)

To our best knowledge, existing solid barriers having different shapes with respect to the straight vertical wall are scarcely investigated in scientific literature so far. Consequently, the parameters driving their design and controlling their performance are unclear. As a consequence of this poor knowledge, designers and inventors have not been adequately supported in devising new SMMs. A 4 m-high straight vertical wall has been proposed as a SMM in the preliminary design of the Segment 1 of the Oman National Railway Network (Italferr, 2014). A 1.5 m-high straight vertical wall has been recently tested in situ along the Mecca-Medina high speed railway in Saudi Arabia (Mendez, 2016), showing insufficient performances. Solid barriers with other geometries have been patented as MMs for different kind of multiphase flows, but their qualitative behavior as mitigation measures has been merely conjectured by the inventors, without rigorous scientific investigation. Murakami and Sakamoto (2001) proposed a vertical barrier with leeward curved free end to shelter highways against windblown snow. Analogously, Guangyong and Peng (2012) patented a leeward inclined barrier with rounded free end to avoid windblown sand sedimentation along railways. Pettus Newell (1903) patented a λ-shaped wood barrier with upwind concavity in order to promote the windblown sand sedimentation upwind the barrier for railway applications. Analogously, Pensa et al. (1990) patented a λ-shaped precast r.c. barrier to be used as SMM for agroforestry applications. Very recently, Bruno et al. (2015) have proposed a novel solid barriers called *Shield for Sand* and patented by Politecnico di Torino. It is equipped with an ad hoc conceived windward concave deflector aimed at making the extent of the upwind eddy and the sand trapping efficiency as large as possible.

In short, four main comments may summarize the above introductory review:

- the results of Hotta and Horikawa (1991) are qualitatively consistent with the wind patterns found by Baines (1963): sedimentation around porous fences is mainly driven by the wind velocity reduction around both surfaces and, to a minor extent, by the wake recirculation region; sedimentation around solid straight vertical wall is conjectured to be mainly driven by the upwind eddy and related reversed flow along the upwind strip;

- generally speaking, porous fences are advisable in dune-building applications, when the fast formation of a bell-shaped dune is pursued and periodic sand removal is not required. Conversely, solid barriers should be preferred as SMM around infrastructures because they involve sedimentation in the upwind strip only, prevent the infrastructure corridor contamination, and allow a safer and cheaper sand removal;

- the quantitative assessment of the effective performance of solid barriers other than the straight vertical wall is needed by infrastructure designers to properly select the most suited design solutions, but it remains an open issue at the present state of the art;

- general design guidelines based on sound aerodynamic principles are needed to inspire the concept of optimal forms for solid barriers.

The present study aims at addressing these open issues by means of a comparative computational study on the aerodynamic behavior of the solid barriers reviewed above. In Section 2 the modeling and computational approach are briefly recalled. The solid barriers selected for the comparative analysis are described in Section 3 together with the far-field wind flow conditions adopted. The results of the analysis are provided in Section 4, while some guidelines for the barrier aerodynamic concept design are proposed in Section 5. Finally, conclusions and perspectives are outlined in Section 6.

2. Wind flow modeling and computational approach

The incompressible, turbulent, separated, steady flow around the barrier is modeled by the classical steady Reynolds Averaged Navier-Stokes (RANS) equations, which, in Cartesian coordinates, read:

$$\frac{\partial \overline{u}_i}{\partial x_i} = 0\,, \tag{1}$$

$$\overline{u}_j \frac{\partial \overline{u}_i}{\partial x_i} = -\frac{1}{\rho}\frac{\partial \overline{p}}{\partial x_i} + \left[\nu\Big(\frac{\partial \overline{u}_i}{\partial x_j} + \frac{\partial \overline{u}_j}{\partial x_i}\Big)\right] - \frac{\partial}{\partial x_j}(\overline{u_i' u_j'})\,, \tag{2}$$

where $\overline{u}_i$ is the averaged velocity, u' the velocity fluctuating component, $\overline{p}$ the averaged pressure, ρ the air density and ν the air kinematic viscosity. The SST $k-\omega$ turbulence model first proposed by Menter (1994) and further modified in Menter et al. (2003) is used to close the T-RANS equations:

$$\overline{u}_j \frac{\partial k}{\partial x_i} = \frac{\partial}{\partial x_i}\left[\Big(\sigma_k \nu_t + \nu\Big)\frac{\partial k}{\partial x_i}\right] + \tilde{P}_k - \beta^* k\omega \tag{3}$$

$$\overline{u}_j \frac{\partial \omega}{\partial x_i} = \frac{\partial}{\partial x_i}\left[\Big(\sigma_\omega \nu_t + \nu\Big)\frac{\partial \omega}{\partial x_i}\right] + \alpha\frac{\omega}{k}P_k - \beta\omega^2 + (1-F_1)\,\frac{2\sigma_\omega}{\omega}\frac{\partial k}{\partial x_i}\frac{\partial \omega}{\partial x_i}, \tag{4}$$

where k is the turbulent kinetic energy, ω its specific dissipation rate and ν_t the so-called turbulent kinematic viscosity. The kinetic energy production term $\tilde{P}_k$ is modeled by introducing a production limiter to prevent the build-up of turbulence in stagnation regions:

$$\tilde{P}_k = \min\left(P_k, 10\beta^* k\omega\right) \quad \text{being} \quad P_k \approx 2\nu_t D_{ij}\frac{\partial \overline{u}_i}{\partial x_i}.$$

For sake of conciseness, the definition of the blending function F_1 and the values of the model constants are omitted herein. Interested readers can find them in Menter et al. (2003). In general, a steady RANS model is adopted having in mind that unsteady fluid phenomena can be neglected to the aims of the present work as sand mass transport happens at a much larger time scale than turbulence characteristic time scales. Indeed, Reynolds Averaged approach has been widely used for a comparable configuration, that is to say dune aerodynamics analysis (Liu et al., 2011; Araújo et al., 2013; Bruno and Fransos, 2015; Lima

et al., 2017). In particular, the SST $k-\omega$ turbulence model is selected for the current application because of its proven accuracy in bluff body aerodynamics in general (Menter et al., 2003) and in the field of dune aerodynamics in particular (Liu et al., 2011; Bruno and Fransos, 2015).
Sand-grain roughness wall functions (Blocken et al., 2007) are used at the ground surface to properly account the effect of its aerodynamic roughness on the incoming wind velocity profile. The equivalent sand grain roughness height is expressed as $k_s = 9.793 z_{0g}/C_s$, where $C_s = 0.5$ is the roughness constant and z_{0g} the aerodynamic roughness of the ground surface.

The adopted 2D computational domain is shown in Figure 4. All the analyzed barriers have an height $h = 4$ m. The barrier height h and the incoming wind speed at its level u_h are adopted in the following as the reference length and velocity, respectively. The length of the axis of the barrier is called l and will be used to evaluate overturning moment.

The computational domain includes the infrastructure cross section, both

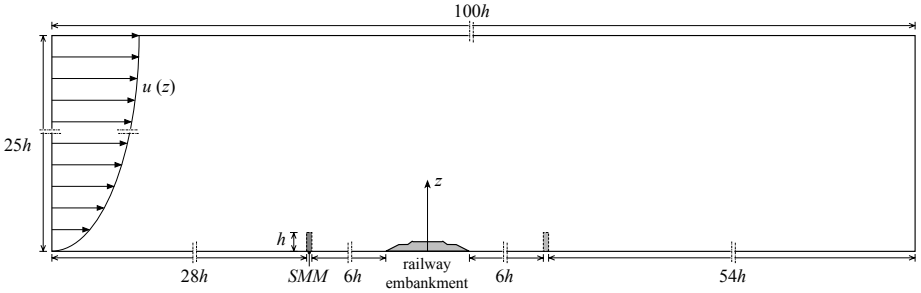

Figure 4: 2D computational domain (not in scale). All the lengths are given in relation to barrier height h. $u(z)$-line represents the incoming logarithmic velocity profile.

the upwind and downwind barriers and the flat ground surface at their surroundings. We indicate as far-field all the quantities incoming, with the aim to model the environmental conditions around the computational domain. The upwind far-field is modeled by means of inlet boundary conditions: a Neumann condition is used for pressure, while Dirichlet conditions are imposed on u, k and ω. The far-field incoming wind velocity profile is prescribed using the log-law $u(z) = \frac{u^*}{k}\log(\frac{z+z_0}{z_0})$, where $k = 0.41$ is the Von Karman constant, $u^* = k\frac{u_{ref}}{\log((h_{ref}+z_0)/z_0)}$ is the friction velocity, $u_{ref} = 18.421$ [m/s] is the mean velocity at height h_{ref} and $h_{ref} = 100$ [m] is the total height of the domain. The value of the far-field aerodynamic roughness z_0 is the object of a parametrical study (see Sect. 3). The profiles of $k(z)$ and $\omega(z)$ are are set in accordance to Richards and Norris (2011) to replicate an external flow. At outlet, if velocity vector points into the domain, the value is fixed to zero, otherwise a zero-gradient condition is imposed. An analogous condition is used for k and ω, while pressure is fixed. No-slip conditions are imposed at the floor surface and at walls.
The Finite Volume open source code OpenFoam© is used to numerically evalu-

ate the flow-field. The space discretization is accomplished by a predominantly structured grid of quadrangular control volumes. Unstructured patterns locally occur at the intersection between the surface-fitted grid boundary layer and the cartesian grid in the higher part of the domain. The mesh is refined near the ground and the barriers in order to get a sufficiently high mesh resolution.

Considering the control volume adjacent to the walls, let be n_p the cell center height. The height of the cell $n_w = 2n_p$ is driven by the sand-grain roughness wall function requirements (Blocken et al., 2007). In particular, n_w should i. provide a sufficiently high mesh resolution in the normal direction n to the surface, ii. comply with the standard requirement on dimensionless wall unit $30 < n^+ = n_p u^*/\nu < 100$, and iii. be longer than twice the sand grain roughness height k_s. The third requirement obeys to the need of avoiding grid cells with centre points within the physical roughness height. Both the second and third requirements limit the grid density at wall. In the following, n_w is set equal to $0.035h$ in order to satisfy at best the above criteria. The n^+ value along the flat surface far upwind and downwind from the barrier is $n^+ \approx 160$, while its value along the barrier surface is smaller than one hundred. The ratio n_p/K_S is larger than unit far from the barrier: hence no significant further grid refinement at wall can be done within the adopted wall treatment. The total number of cells is around 16000, depending on the barrier geometry. The cell-centre values of the variables are interpolated at face locations using the second-order Central Difference Scheme for the diffusive terms. The convection terms are discretised by means of the so-called Limited Linear scheme, a 2nd order accurate bounded Total Variational Diminishing (TVD) scheme resulting from the application of the Sweby limiter (Sweby, 1984) to the central differencing in order to enforce a monotonicity criterion. The SIMPLE scheme is used for pressure-velocity coupling.
The whole adopted computational model described above has been validated against accurate wind tunnel tests in Bruno and Fransos (2015) for the same class of aerodynamic problems, i.e. a nominal 2D bluff body immersed in a turbulent boundary layer.

3. Set-up of comparative analysis

The aerodynamic behavior and related performances of windblown sand barrier are expected to be affected by two main factors: the geometry of the barrier profile and the far-field incoming wind velocity profile. Having this in mind, the comparative analysis develops in two steps.

First, the effects of the geometry of six solid barriers are discussed. The basic Straight Vertical Wall (VSW) already studied by Baines (1963) is retained as a reference. Its aerodynamic performances are compared with four barriers inspired to patents already proposed for windblown sand or snow (Guangyong and Peng, 2012; Pettus Newell, 1903; Pensa et al., 1990; Murakami and Sakamoto, 2001), and with the new Shield for Sand (S4S) barrier (Bruno et al., 2015). For the sake of conciseness, patented barriers are referred to by the patent country code. The analyzed barrier profiles are shown in Figure 5. The barriers mainly

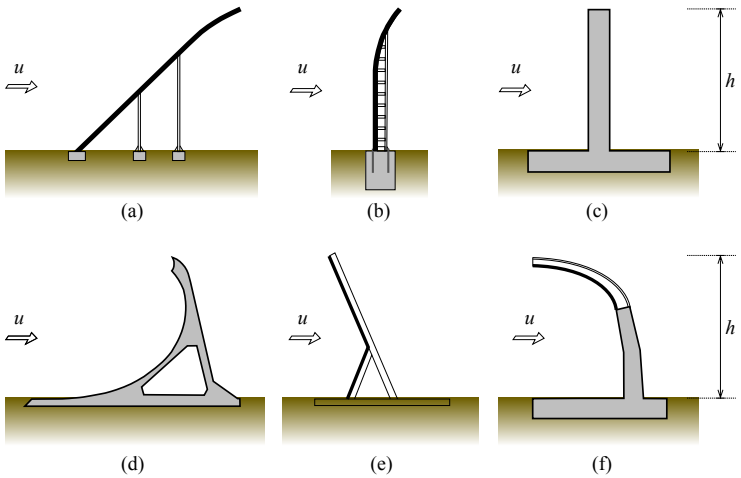

Figure 5: Barrier profiles analyzed and executive details: a) Guangyong and Peng (2012) (CN), b) Murakami and Sakamoto (2001) (JP), c) Straight Vertical Wall (SVW), d) Pensa et al. (1990) (IT), e) Pettus Newell (1903) (US), f) Bruno et al. (2015) (S4S)

differ among them by their inclination with respect to the incoming wind, i.e. downwind free end barriers (CN and JP) or windward free end barriers (IT, US and S4S), and by the shape of their profiles. They are arranged in Figure 5 for increasing inclination against the incoming wind. In particular, a rendering of the S4S barrier is shown in Figure 6. The streamlines of the simulated flow field around the barrier, the railway embankment and a train are included to shed some light on the principles of its concept design.

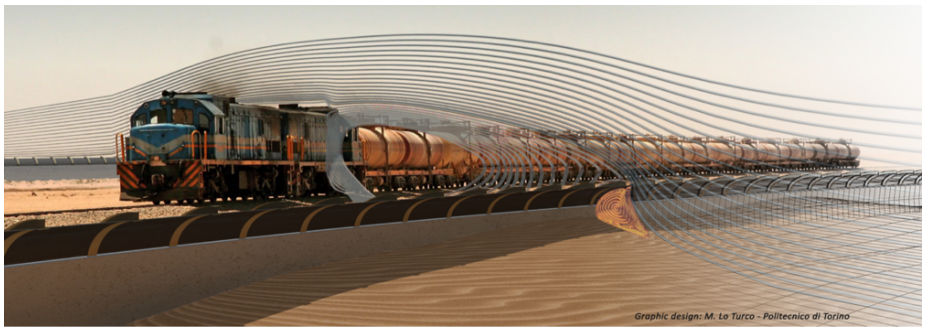

Figure 6: Rendering of the S4S barrier along a railway. Simulated streamlines overcoming S4S barrier are grey colored, the upwind trapping vortex is gold colored.

The main idea underlying the S4S barrier is to take advantage of its effects on the local wind field in order to promote the sand sedimentation in the upwind strip only, preventing sedimentation in the infrastructure corridor (Figure 1). The barrier profile, and in particular the deflecting upper part, is designed to

make the extent of the eddy with horizontal axis upwind the barrier (highlighted in yellow in fig. 6) as large as possible. The reversed flow is expected to strongly reduce the velocity gradient close to the ground surface. The shear stress and the friction velocity are presumed to decrease as well. Windblown sand sedimentation is expected to be promoted in turn on the ground surface where the friction velocity u^* is lower than its erosion threshold value u_t^* . Hence, qualitatively speaking, the larger the upwind eddy, the higher the barrier trapping capacity, i.e. the volume of sedimented sand at which sand removal is required. In this sense, the upwind eddy acts in SM application as a sand trapping vortex. Other design targets are: cheap and effective maintenance by fully compliant existing sand removal machines, e.g. the Santera 3000© sand cutter and blower (Schmidt, 2013); high durability of the building elements; simple prefabricated building elements, possibly already employed in the industrial chain of other kinds of barriers, e.g. noise or wind barriers.
The ground surface along the sides of line-like infrastructures, e.g. railways or roads, is usually flattened for construction and maintenance purposes, therefore ground features can be considered uniform in this zone. Far-field ground features vary along the alignment instead. In order to reflect this actual ground surface conditions, the ground surface in the computational domain is splitted according to the scheme in Figure 7. The infrastructure side corridor includes

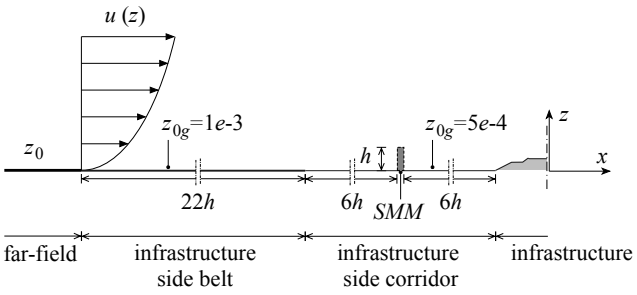

Figure 7: Aerodynamic roughness changes along the domain (not in scale). The sub-index g stands for ground, which means z_{0g}, is the roughness length used by the wall functions in that part of the domain.

the safety and maintenance road. It usually consists of stabilized smoothed surfaces. The related aerodynamic roughness is expected to be low and set in the following $z_{0g} = 5e - 4$ [m].s The infrastructure side belt is bulldozed by earth-moving machinery. Its aerodynamic roughness is expected to be higher than in the side corridor and set in the following $z_{0g} = 1e - 3$ [m]. In the barrier geometry comparative analysis, the far-field aerodynamic roughness is kept constant $z_0 = 1e-2$ [m]. The far-field friction velocity is set $u^* = 0.82$ [m/s], in order to exceed the mean value of the fluid threshold shear velocity u_t^* for every value of the sand grain diameter d in the range $0.063 \leq d \leq 1.2$ [mm] (Raffaele et al., 2016), characteristic of the desert. It follows $Re_h = hu_h/\nu = 3.3e + 6$.

Second, two barriers are selected, namely SVW and S4S, and the effects

of different far-field aerodynamic roughness on their aerodynamic behavior are discussed. These effects are expect to be significant according to Baines (1963) pioneering tests. Moreover, the study allows to discuss the barrier performances under different site environmental conditions. Uniform flow, i.e. $u(z) = cnst$ is simulated by removing the no slip boundary condition at the ground surface, in order to replicate the experimental conditions adopted by Baines (1963) (Fig. 2-b). Log-profiles are obtained by setting different values of the far-field aerodynamic roughness length $z_0 = [5e-4, 1e-3, 5e-3, 1e-2, 5e-2]$ [m]. The highest value approximates the one adopted by Baines (1963) (Fig. 2-a), while the range $1e-3 \leq z_0 \leq 1e-2$ [m] is representative of actual conditions in deserts. The far-field friction velocity $u^* = 0.82$ [m/s] is kept constant in every condition, in order to vary a single parameter in the incoming wind velocity log-law. This value involves a wall shear stress $\tau = {u^*}^2\rho > \tau_t = {u_t^*}^2\rho$ for every value of the far-field aerodynamic roughness length z_0. Consequently, u_h varies with z_0. This, in turn, affects the Reynolds number $Re_h = hu_h/\nu$, which slightly varies in the range $2.5e+6 \leq Re_h \leq 5e+6$. Significant Re effects are not expected in this range, because of the bluffness of the barriers and the high Re number. In other words, the scrutinized Re interval entirely lies in the post critical regime.

4. Results

In this section, results obtained in the two comparative studies described above are separately discussed.

4.1. Effects of barriers geometry

In this section we analyze the effects of barrier geometry on flow patterns and consequently on aerodynamic and sedimentation performances.

First, we *qualitatively* analyze the flow patterns upwind and downwind the barriers in order to better understand their effects on the local wind flux. Figure 8 collects the simulated mean streamlines around the adopted barriers. The upwind trapping vortex induced by each SMM is pointed out by a light blue field. In Sect. 1 we have assumed this flow structure to be the main cause of the sand sedimentation around solid barriers. This same flow structure results to be by far the most sensitive to the barrier geometry. In Figure 8 barriers are arranged by increasing order of the trapping vortex area. CN and JP barrier profiles promote the upward deflection of the flow due to their leeward free ends, and reduce the size of the upwind trapping vortex in turn. These adverse effects are amplified by the windward foot of CN and IT. Upwind trapping vortices larger than the one induced by the reference SVW are obtained by barriers with a pronounced windward free end, that is US and S4S . However, the limited extension of the windward free end in IT does not counteract the adverse effect of its long windward foot. In particular, the windward curved panel at the top of the S4S barrier promotes the local downward deflection of the flow upwind the barrier, and the formation of the largest trapping vortex.

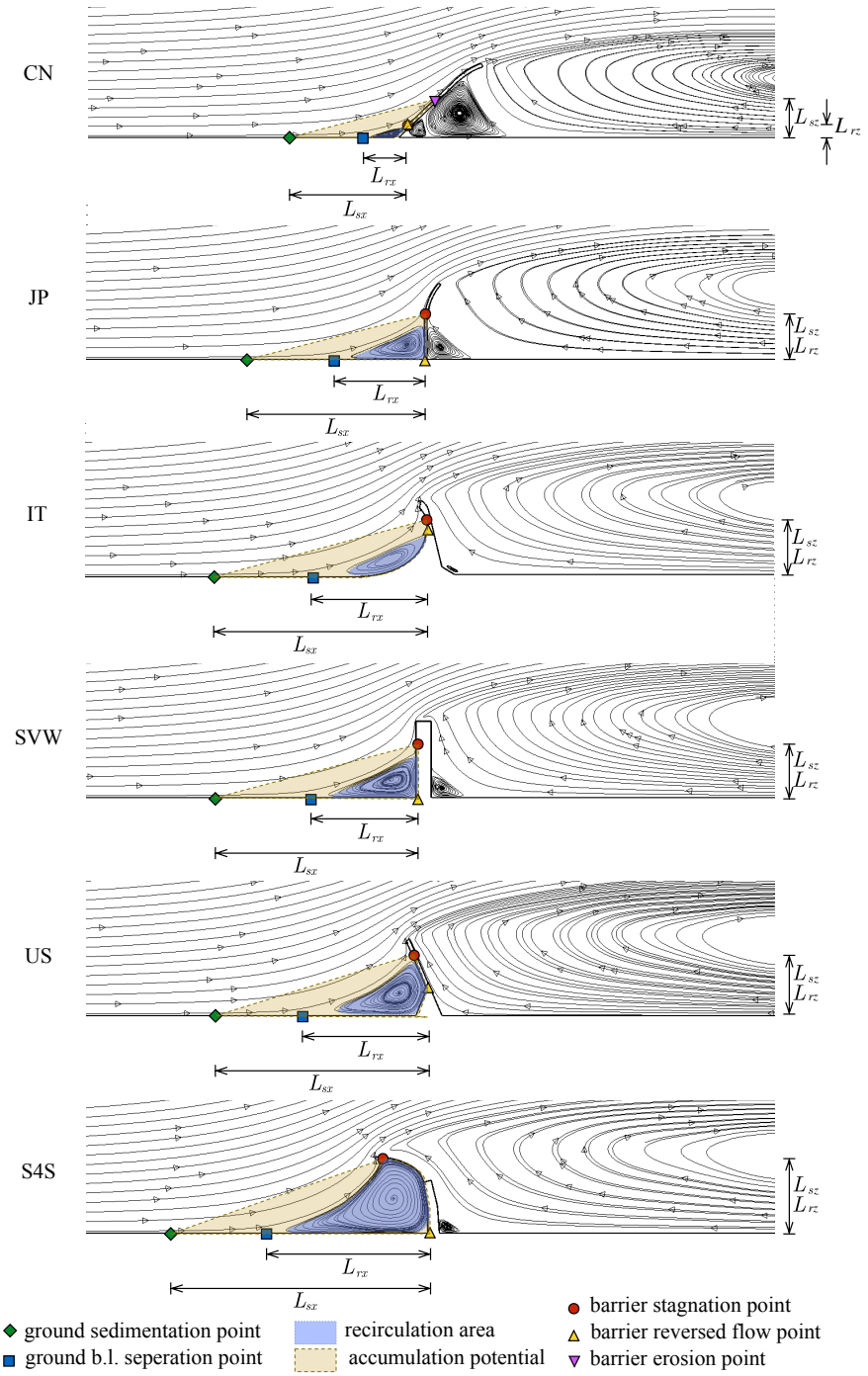

Figure 8: Mean streamlines around barriers, structures and characteristic lengths of the local flow. The area of the upwind recirculation vortex is blue-filled, while the accumulation potential area is yellow-filled in order to distinguish between the two metrics used in the barriers performance analysis.

In order to *quantitatively* analyze SMM performances, let us introduce some remarkable points along the ground upwind strip and the barrier forebody (Fig. 8). They are defined with respect to the wall shear stress τ:

- the stagnation point on the barrier front surface St_b (x_{st}, z_{st}), classically defined as the point where $|\tau| = 0$;
- the point on the barrier front surface where reversed flow takes place R_b (x_{rb}, z_{rb}), defined as the point where the x-component of the wall shear stress $\tau_x = \mu \frac{\partial u}{\partial x}|_{z=0} = 0^+$, i.e. where τ_x switches from positive to negative values;
- the separation point of the ground boundary layer along the upwind strip surface R_g $(x_{rg}, 0)$, defined as the point where $\tau_x = 0$;
- the sedimentation point on the ground upwind strip surface S_g $(x_{sg}, 0)$, defined as the point where $|\tau| = \tau_t$; i.e. where sedimentation of the incoming windblown sand starts;
- the erosion point on the barrier front surface E_b (x_{eb}, z_{eb}), defined as the point where $|\tau| = \tau_t$ i.e. where erosion of the incoming windblown sand takes place. This point lies between the stagnation point and the separation point at the barrier free end. Due to the high flow acceleration in this region, the barrier erosion point is very close to the stagnation point, except for CN.

Hence, we can define some characteristic lengths of the local flow and sedimentation around the barrier forebody:

- recirculation x-length: $L_{rx} = |x_{rb} - x_{rg}|$, i.e. the along-wind projection of the trapping vortex;
- recirculation z-length: $L_{rz} = |z_{st}|$, i.e. the vertical projection of the trapping vortex;;
- sedimentation x-length: $L_{sx} = |\max(x_{rb}, x_{eb}) - x_{sg}|$, i.e. the along-wind projection of the ground and barrier profiles where sedimentation occurs;
- sedimentation z-length: $L_{sz} = |z_{eb}|$, i.e. the vertical projection of the ground and barrier profiles where sedimentation occurs.

The above lengths are drawn for each barrier in Figure 8. We point out that recirculation lengths depend on the aerodynamic setup only, while sedimentation lengths depend on the sand grain diameter too, being $\tau_t(d)$ (Raffaele et al., 2016). Figure 9 graphs the couple L_{sx} - L_{rx} for three different values of the grain diameter and for each barrier.

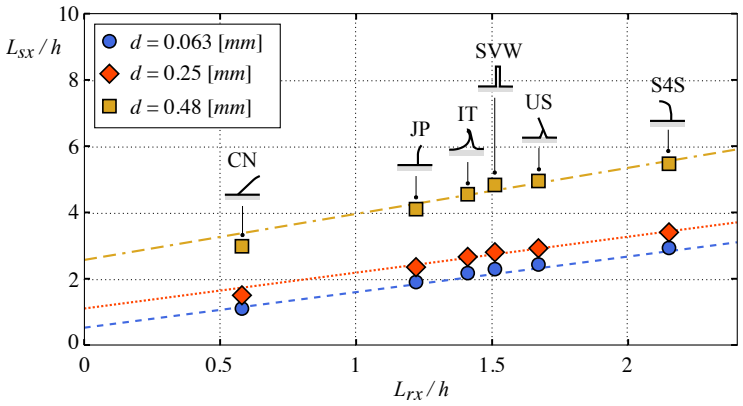

Figure 9: Sedimentation - recirculation x-lengths for different grain diameters and barriers analyzed; linear dependence between these characteristic lengths for each grain size d.

First, the recirculation x-length and the sedimentation x-length are clearly proportional. In other words, for a given incoming flow profile, the longer the recirculation x-length, the longer the sedimentation one. The same proportionality does not hold between recirculation and sedimentation y-lengths, where the barrier profile plays a predominant role. Second, the larger the sand grain diameter, the higher the fluid threshold shear velocity, the longer the sedimentation x-length.

Finally, we define the aerodynamic recirculation area $A_r \propto L_{rx}L_{rz}$ as the area of the trapping vortex (light blue fields in Fig. 8), and the sand accumulation potential $A_s \propto L_{sx}L_{sz}$ (light yellow fields in Fig. 8). The exact evaluation of A_s would require the rigorous simulation of a multiphase flow (air and sand) with free surface (the accumulated sand profile upwind the barrier) up to its equilibrium condition. This issue, although very interesting and challenging in a purely scientific perspective, is out of scope in a conceptual design phase. In order to encompass this problem, the free surface at equilibrium is approximated as the straight segment between the ground sedimentation point and the barrier erosion point (see Fig. 8). The above approximated definition of the free surface and A_s allows a preliminary estimate of the SMM sedimentation performance during its conceptual design on the basis of purely aerodynamic studies, that is without including sand in Wind Tunnel tests or Computational Wind Engineering simulations. Even if the sedimentation performance metric is expected to be roughly evaluated, the relative performances of different candidate solutions is valid in a conceptual design perspective. A_r and A_s for $d = 0.25$ [mm] are plotted in their dimensionless form in Figure 10.

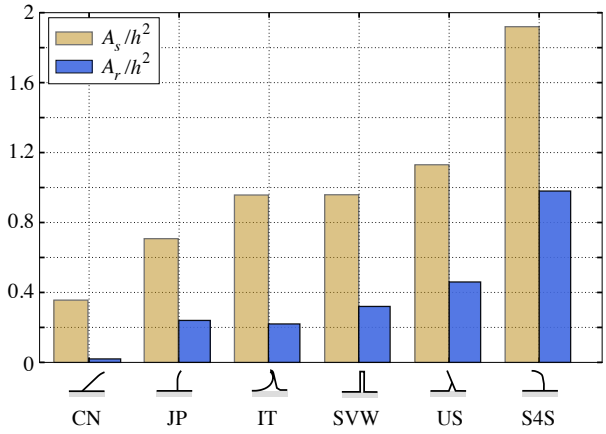

Figure 10: Normalized recirculation area A_r and accumulation potential A_s of the analyzed barriers. The barriers are sorted by ascending sedimentation performance growth.

S4S shows the biggest improvement with respect to SW. It is interesting to note that CN and JP show a worse potential behavior; actually JP has been designed for windblown-snow and there is no reason to state that it should work for windblown-sand as well. Both configurations actually have different geometrical aspects (examined in details in next sessions) which negatively influence performances, both for sedimentation (A_s) and in aerodynamics terms (A_r). Windblown sand barriers are mainly addressed to promote sedimentation, so that accumulation potential A_s is they driving performance metric. However, their design also depends on wind-induced loads. In order to comparatively evaluate them, the profiles of the mean value of the pressure coefficient $\overline{C}_p = \frac{\overline{p}-p_\infty}{1/2\rho u_h^2}$ are plotted in Figure 11 (a) and (b) along the front and rear surfaces of the barriers, respectively. $\overline{p}$ is mean pressure and p_∞ is the freestream pressure .

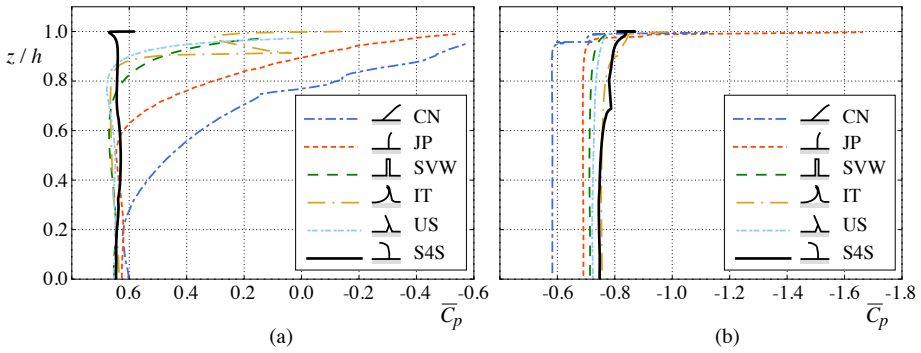

Figure 11: $\overline{C}_p$ distribution along front surface (a) and rear surface (b) of the analyzed barriers

The pressure field is closely related to the flow field (Fig. 8). The maximum value of $\overline{C}_p$ corresponds to the stagnation point on the front surface (red bullets

in Fig. 8). The pressure is nearly constant along L_{rz} for all barriers, i.e. along the portion of the front surface facing to the upwind trapping vortex. Because of this, the pressure distribution is constant along the whole front surface of S4S barrier. The downward free-end of CN and JP barriers promotes the upward deflection of the flow, and the wind speed growth. The higher the local wind speed, the lower the pressure along the front surface (Fig. 11-(a), CN and JP curves), consistently with the Bernoulli law. Finally, the non monotonic trend along IT front surface is due to the its scimitar-shaped upper part. The $\overline{C}_p$ distribution along the rear surface is nearly constant for all barriers. This is because of the large recirculation region in their wake. As pointed out in studies on fundamental bluff body aerodynamics, e.g. in Bruno et al. (2014), the mean pressure value on the body base surface is directly related to the curvature of the time-averaged flow streamlines around the same surface, and, in particular, to the shape and length of the main recirculation region. As one can see in Figure 8, the streamlines in the wake are very similar for all the barriers, except for CN and, in a minor extent, for JP. For these barriers, the shape of the leeward free-end induces a lower z-component and an higher x-component of the wind velocity at the separation point. This involves a flatter and more elongated shape of the recirculation region in the wake, and a higher suction along the rear surface in turn. In order to provide a synthetic aerodynamic performance metrics for conceptual design purposes, we finally evaluate the mean value of the moment coefficient $\overline{C}_M = \frac{\overline{M}}{1/2\rho u_h^2 L^2}$ for the different barriers. M is evaluated at the contact point between the ground and the front surface, i.e. it is the aerodynamic overturning moment. L is a suitable reference length: we alternatively adopt both the barrier height h, and the barrier section axis length l. Figure 12 collects the mean moment coefficients of the analyses barriers. For the sake of comparison, the mean value of each barrier is further normalized with respect to the one acting on Straight Vertical Wall, adopted as reference case.

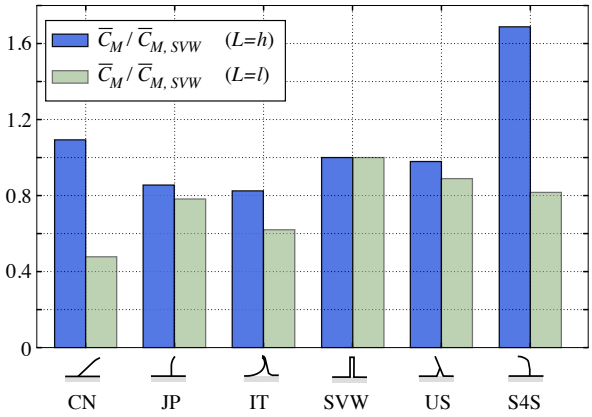

Figure 12: Normalized overturning aerodynamic moment for the analyzed barriers. Normalization has been performed using two different characteristic lengths L: the barrier height h (dark blue histograms) and the length l of the axis of the barrier section (light green histograms).

C_M depends on the position of the aerodynamic center and on the aerodynamic force components, that result in turn from pressure distribution on the barrier surface. $L = h$-scaling of the aerodynamic moment, $C_M(h)$ in short, is the common practice for wall-mounted bodies with straight normal axis. In this case, barriers whose axis significantly departs form vertical show the highest $C_M(h)$, notably CN and S4S barriers. In particular, the sought-after sedimentation performance of S4S is accompanied by an unwanted high wind action. These performances are necessarily coupled, because they follow from a common flow feature. The large upwind trapping vortex induces on the one hand the large sedimentation potential A_s, and on the other hand a constant pressure distribution along the front surface (see Fig. 11-a). The aerodynamic center moves upwards in turn, and both the drag and lift force components contribute to clockwise overturning moment. Even if $C_M(h)$ provides a sound comparison of the overturning moments, $L = h$-scaling does not account for the different development of the barrier surface along which the pressure is applied. Conversely, $L = l$-scaling weights for aerodynamic moment with the length of the barrier axis, as an averaged measure of the extent of front and rear surfaces. In this case, SVW is subjected to the highest $C_M(l)$, while, all barrier heights being equal, the further from vertical the barrier axis, the smaller $C_M(l)$.

4.2. Effects of the far-field aerodynamic roughness

In this section we examine the impact of the far-field aerodynamic roughness on the flow pattern around barriers, and related performances as well. The obtained results are presented and discussed analogously to what we have done in the previous comparative analysis. We start by a *qualitative* analysis of the flow structures: Figure 13 compares the simulated mean streamlines around SVW and S4S barriers for different values of the aerodynamic roughness z_0 and

related incoming wind velocity profiles. The aerodynamic recirculation area and the sand accumulation potential are pointed out, together with related critical locations and characteristic lengths. The simulated flow patterns around SVW qualitatively agree with the one early sketched by Baines (1963) (Fig. 2), even if the simulated free boundary of the upwind recirculation area is slightly concave rather than highly convex, and $L_{rx} > Lry$. The recirculation area takes place upwind both barriers even for the lowest simulated $z_0 = 5e{-}4$ m, and its lengths L_{rx}, L_{rz} slightly vary versus the aerodynamic roughness. However, the sedimentation x-length L_{sx} of both barriers strongly depends on the aerodynamic roughness: the higher z_0, the longer L_{sx}.

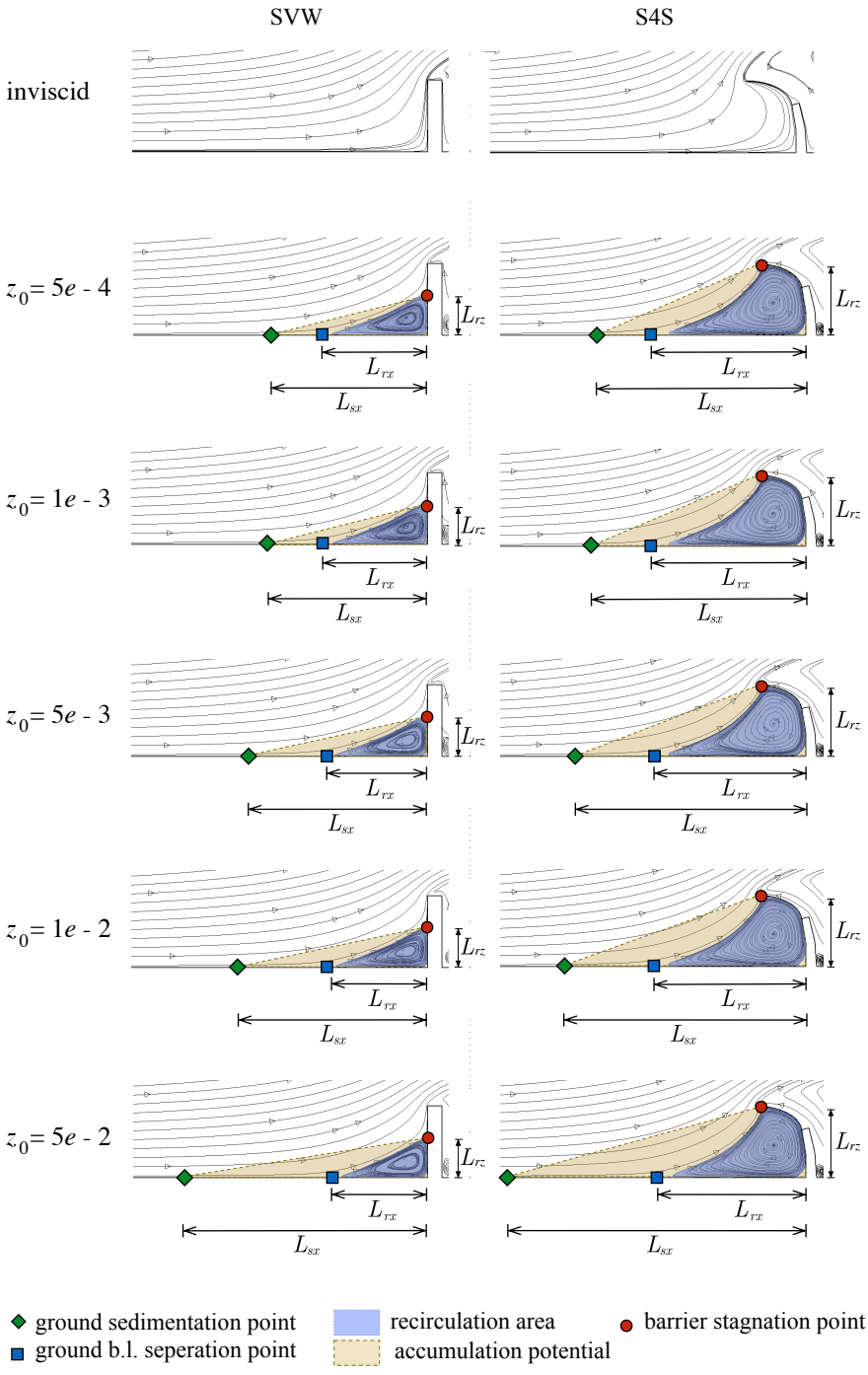

Figure 13: Mean streamlines around SVW and S4S barriers for different far-field aerodynamic roughness z_0.

In order to *quantitatively* analyze the barrier performances for different far-field aerodynamic roughness, Figure 14 graphs the recirculation x-length L_{rx} and sedimentation x-length L_{sx}, both normalized by the barrier height.

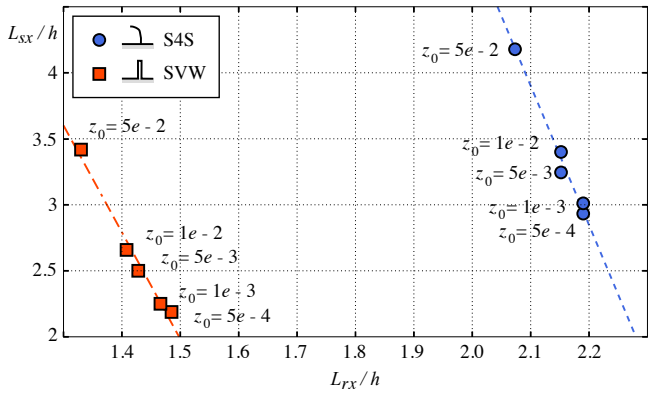

Figure 14: Sedimentation - recirculation x-lengths for different far-field aerodynamic roughness z_0. Linear trends are highlighted by means of dotted lines.

Recirculation and sedimentation lengths of the S4S barrier are larger than SVW ones for every adopted value of z_0 ($L_{rx,SMaRT} \approx 1.5L_{rx,SVW}$, $L_{sx,SMaRT} \approx 1.3L_{sx,SVW}$). In spite of this, both barriers share a common trend: the recirculation x-length and the sedimentation x-length are inversely proportional. In other words, for a given barrier, the larger the aerodynamic roughness z_0, the longer L_{sx} and the shorter L_{rx}.

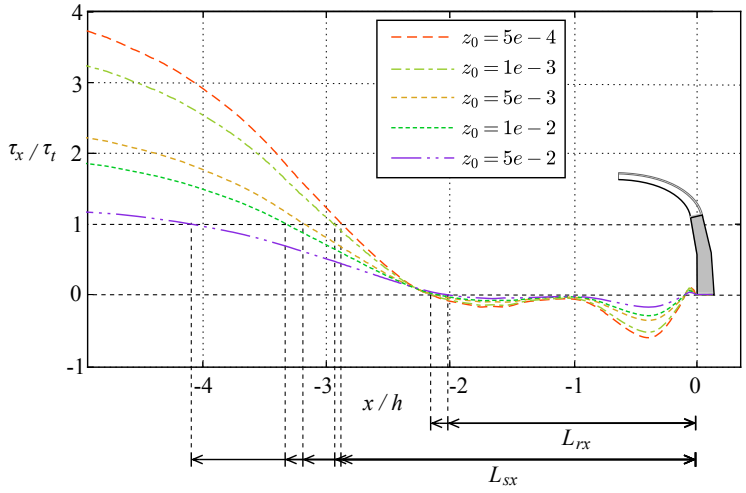

Figure 15: Shear stress τ_x along the upwind strip for different far-field aerodynamic roughness z_0. The curves have been normalized by means of threshold shear stress τ_t.

In order to shed some light on this counter-intuitive result, in Figure 15 we report the wall shear stress τ_x profile along the ground strip surface upwind the S4S barrier. The wall shear stress is normalized with respect to τ_t for the sake of clarity. L_{rx} corresponds to the distance from the barrier foot up to the point where $\tau_x/\tau_t = 0$ (lower horizontal dashed grid line in Fig. 15). High values of z_0 reduce the curvature of the attacking velocity profile, and slightly reduce its size as a consequence. L_{sx} corresponds to the distance from the barrier foot up to the point where $\tau_x/\tau_t = 1$ (upper horizontal dashed grid line in Fig. 15). High values of z_0 reduce the z-derivative of the far-field wind velocity profile and the corresponding shear stress in turn, being $\tau_x \propto \frac{\partial u}{\partial z}|_{z=0} = \frac{u^*}{kz_0}$. Despite the changes of z_{0g} along the infrastructure corridor, this reduction has an impact on the ground shear stresses just upwind the barrier. It follows that the erosion potential is reduced for increasing z_0 (see e.g. τ_x/τ_t at $x/h = -5$), leading to a long sedimentation length. In order to quantitatively assess the barrier performances versus the far-field aerodynamic roughness z_0, dimensionless A_r/h^2 and A_s/h^2 are graphed in Figure 16 versus the dimensionless ratio $u^*/u_h = \frac{k}{\log((h+z_0)/z_0)}$.

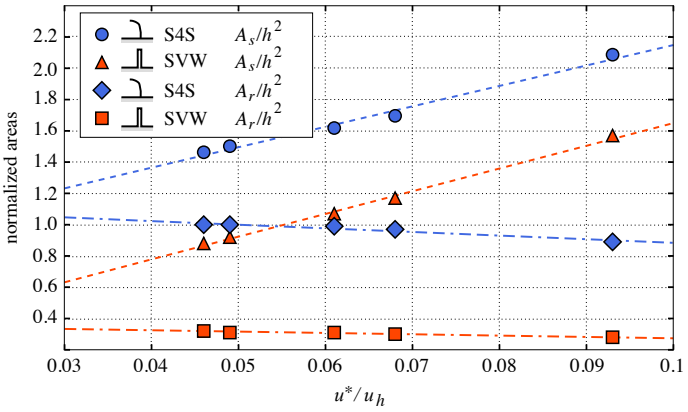

Figure 16: S4S and SVW recirculation area and accumulation potential for different far-field aerodynamic roughness z_0. Linear trends are highlighted by means of dotted lines.

Since L_{sx} significantly increases with z_0, potential accumulation increases as well. Analogously, since L_{rx} slightly decreases with z_0, recirculation area is reduced in the same way. Both trends can be approximated as linear. Their slopes allow to consider A_r constant versus u^*/u_h, to a first approximation.

For the sake of conciseness, the sensitivity of the overall wind load on the barriers to the far-field roughness is not discussed herein. In the following, the analysis is limited to the relationship between the pressure trend along the barriers and the local flow field induced by the far-field roughness. The pressure along the rear surface is nearly constant (Figure 11-b). Hence, we focus on the pressure distribution along the front surface only. For each set-up, pressure is scaled with respect to the corresponding far-field wind velocity u_h, and each

resulting $\overline{C}_p$ profile is further normalized by its maximum value. In other words, we refer to the normalized pressure coefficient distribution $\overline{C}_p/\overline{C}_{p,max}$, in order to point out the trend rather than the pressure magnitude. Figure 17 collects the profiles for both barriers and for each far-field roughness. Computational profiles along SVW are compared with the experimental profiles obtained by Baines (1963), Good and Joubert (1968) and Letchford and Holmes (1994).

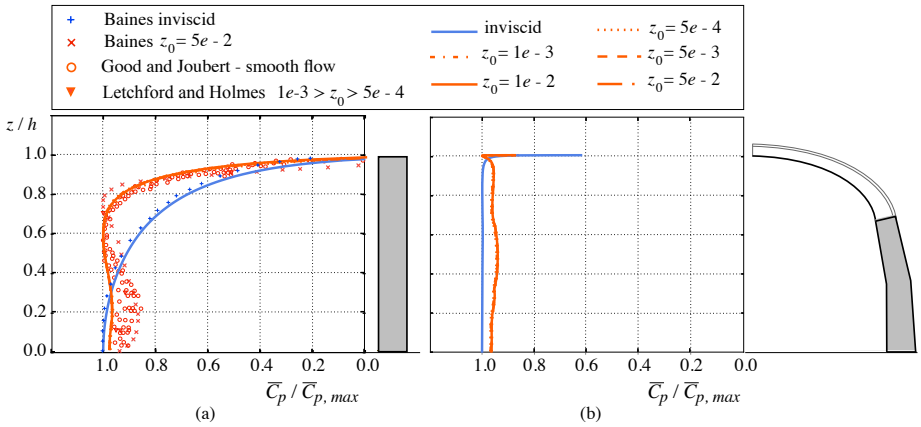

Figure 17: $\overline{C}_p/\overline{C}_{p,max}$ coefficient along front surface of SVW (a) and S4S barrier (b) for different far-field aerodynamic roughness. The normalized profiles are compared with the experimental results in Baines (1963), Good and Joubert (1968) and Letchford and Holmes (1994) .

The trend of the normalized pressure distribution significantly differs for inviscid and viscous conditions in both experiments and simulations. The differences are more evident along SVW. In the inviscid condition the trend is monotonically decreasing, i.e. the local flow progressively accelerates toward the free end. In the viscous condition the trend is no longer monotonic and the stagnation point, i.e. $\overline{C}_p/\overline{C}_{p,max} = 1$ at about $z/h = 0.65$ for every aerodynamic roughness, is the watershed between the lower reversed flow and the upper accelerated flow. The normalized pressure distributions along S4S are nearly constant for both inviscid and viscous conditions, i.e. the whole front surfaces are immersed in the same flow topology: upward deflected flow in inviscid condition, and reversed flow in viscous condition. The distributions along SVW obtained by computational simulations quite agree with the experimental ones. The matching is almost perfect for the inviscid flow in Baines (1963). In viscous flow setups, the trend of experimental measurements slightly depends on the aerodynamic roughness and related incoming wind velocity profile, while the simulated pressure distributions have the same trend. We conjecture this is due to the effect of the ground aerodynamic roughness along the infrastructure belt and corridor, which is kept constant in every simulation, and which locally modifies the far-field incoming wind.

5. Guidelines fo aerodynamic conceptual design

In this section we aim at proposing some guidelines in the perspective of the aerodynamic conceptual design of windblown sand solid barriers. The guidelines are intended to provide a synthetic, necessarily approximated assessment of the sedimentation performance. The guidelines are intended to move from the physical reading of the aerodynamic behavior of the investigated barriers towards more general criteria.

We have previously highlighted the significant role played by barrier geometry and far-field aerodynamic roughness. Let us briefly summarize the main qualitative working principles we have recognized about these set-up features: i. windward free end promotes the local downward deflection of the flow upwind the barrier, and the formation of the trapping vortex; ii. leeward free end and windward foot promote the upward deflection of the flow, and reduce the size of the trapping vortex; iii. the far-field aerodynamic roughness increases the accumulation potential.

Concerning the *geometry*, some kind of idealization is needed to reduce the very different and complex barrier profiles to simple and general working-features. Therefore, we approximate the profile by two straight line segments, representative of the two mean slopes of the barrier profile. These segments are obtained using a least-squares method applied to two sets of points belonging to the barrier profile. These two sets contain all the points of the front face profile having same slope sign of tangent line each. In this way, the two straight line segments approximations carry informations regarding the curvature of the barrier, bearing in mind the items i. and ii. above. Figure 18 shows the IT approximation as an example of the proposed procedure.

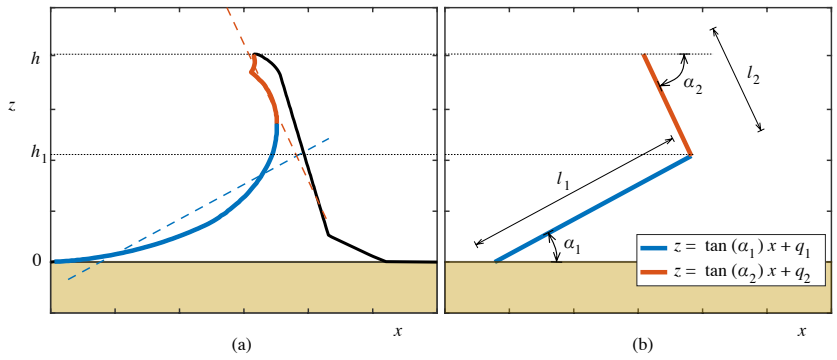

Figure 18: Barrier idealization: (a) original IT profile, (b) 2 straight line-segment profile. Segment profile is obtained by means of a least-squares approximation technique.

This approximation generalizes and reduces a complex profile shape to essentially five design parameters: the angle between ground line and first line-segment α_1, the angle between second line-segment and a virtual horizontal straight line α_2, the height of the two straight lines intersection h_1, the lengths

of the two line-segments l_1 and l_2 .

Concerning the effect of the *far-field aerodynamic roughness*, a linear relation between the ratio $\frac{u^*}{u_h}$ and the accumulation potential has been observed. By using these design variables, we heuristically define the empirical dimensionless estimator

$$\gamma = \left(\frac{h}{h-h_1} \frac{l_2}{h} \cos\alpha_2 - \frac{h-h_1}{h} \frac{l_1}{h} \cos\alpha_1 \right) \frac{u^*}{u_h} \tag{5}$$

to relate barrier geometry and incoming wind profile to sedimentation performance. The first term in brackets model the positive effect of the windward free end ($\cos\alpha_2 > 0$, i.e. $0 < \alpha_2 < 90$) on sedimentation. The second term model the adverse effect of the windward foot ($-\cos\alpha_1 < 0$, i.e. $0 < \alpha_1 < 90$). Both terms include the length of the corresponding straight line-segment. It is clear that $\gamma = 0$ for SVW, whichever is the far-field aerodynamic roughness. Hence, we conjecture the accumulation potential of a barrier can be expressed as

$$A_s \approx A_{s,SVW}(1 + a\gamma), \tag{6}$$

where a is a parameter that we expect depends on the width and aerodynamic roughness of the infrastructure corridor and belt. Figure 19 collects the pairs (γ, A_s) related to the barrier geometries and roughness lengths considered in the study: the values of γ are obtained by Eq. 5, while A_s values result from the previous computational simulations, and are scaled by the accumulation potential of SVW. The linear trend of the data confirms the conjectured relation in Eq. 6. The linear fitting of the data by Eq. 6 gives $a = 5.7$ (R-squared $R^2 = 0.985$).

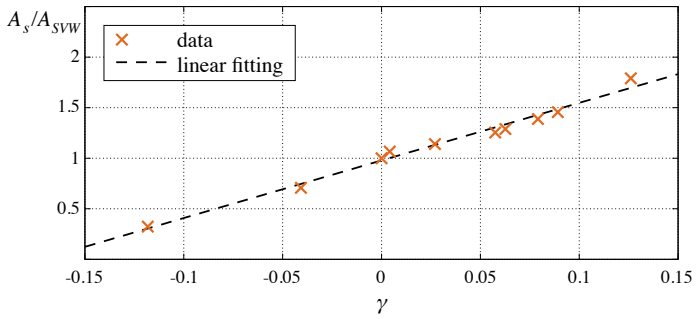

Figure 19: γ-A_s data and linear fitting to Eq. 6

It is worth stressing that this relation is a crude simplification of nonlinear aerodynamic phenomena, and it is not a rigorously derived reduced order model. However it offers to designers some physical-based, range-finding, time-saving indications useful in the conceptual design. It should be further complemented by accurate computational simulations, wind tunnel tests and full-scale field trials in the subsequent design stages.

6. Conclusions

The present study critically compares the aerodynamic behavior of different windblown sand barriers proposed in scientific and technical literature so far. The sand sedimentation performance of each barrier is estimated by an approximated metric in the perspective of its use in conceptual design. In the same perspective, some guidelines to conceptual design of windblown solid barriers are proposed on the basis of the phenomenological analysis of the obtained results.

The patented S4S barrier shows the best sedimentation performances thanks to its innovative aerodynamic shaping. These performances are necessarily accompanied by the growth of the mean wind-induced overturning moment. We hope this study sheds some light in the main working principles of windblown sand solid barriers, provides guidance to designers, and allows the proper choice of Sand Mitigation Measures along infrastructures.

More accurate approaches to windblown sand modelling and SMM performance assessment are still to be developed to meet the engineering needs during detailed and as built design. These tools includes, among others, i. multiphase wind-sand computational models able to simulate the dynamics of wind, saltating sand and sand accumulation/erosion profile, ii. wind tunnel testing procedure to fulfill similarity requirements about both barrier, wind and sand saltation layer, iii. accurate and durable measurement techniques to be adopted during long-term field trials.

Acknowledgments

The study has been developed in the framework of the Windblown Sand Modeling and Mitigation (WSMM) joint research, development and consulting group established between Politecnico di Torino and Optiflow Company. The authors wish to thank Luigi Preziosi, member of the WSMM group and coinventor of the S4S barrier, for the helpful discussions about the topics of the paper. Computational resources were provided by HPC@POLITO, a project of Academic Computing within the Department of Control and Computer Engineering at the Politecnico di Torino (http://www.hpc.polito.it). The S4S patent is funded and managed by the Technology Transfer and Industrial Liaison Department of Politecnico di Torino.

References

Alghamdi, A.A., Al-Kahtani, N.S., 2005. Sand control measures and sand drift fences. Journal of Performance of Constructed Facilities 19, 295–299.

Araújo, A., Parteli, E., Pöschel, T., Andrade, J., 2013. Numerical modeling of the wind flow over a transverse dune. Scientific Reports 3 2858, 1–9.

Baines, W., 1963. Effects of velocity distribution on wind loads and flow patterns on buildings, in: Proceedings of Conference "Wind effects on buildings and structures", National Physical Laboratory. pp. 198–225.

Blocken, B., Stathopoulos, T., Carmeliet, J., 2007. Cfd simulation of the atmospheric boundary layer: wall function problems. Atmospheric Environment 41, 238 – 252.

Bofah, K., Al-Hinai, K., 1986. Field tests of porous fences in the regime of sand-laden wind. Journal of Wind Engineering and Industrial Aerodynamics 23, 309–319.

Bofah, K., Kramer, C., Gerhardt, H., 1991. Design considerations for buildings in sandy and dusty environment. Journal of Wind Engineering and Industrial Aerodynamics 38, 161–166.

Bruno, L., Fransos, D., 2015. Sand transverse dune aerodynamics: 3d coherent flow structures from a computational study. Journal of Wind Engineering and Industrial Aerodynamics 147, 291 – 301.

Bruno, L., Preziosi, L., Fransos, D., 2015. A deflecting module for an anti-sand barrier, a barrier thus obtained and a protection method from windblown sand - Patent number PCT/IT2015/000169.

Bruno, L., Salvetti, M.V., Ricciardelli, F., 2014. Benchmark on the aerodynamics of a rectangular 5:1 cylinder: an overview after the first four years of activity. Journal of Wind Engineering and Industrial Aerodynamics 126, 87–106.

Cheng, J., Jiang, F., Xue, C., Xin, G., Li, K., Yang, Y., 2015. Characteristics of the disastrous wind-sand environment along railways in the Gobi area of Xinjiang, China. Atmospheric Environment 102, 344 – 354.

Cheng, J., Xue, C., 2014. The sand-damage prevention engineering system for the railway in the desert region of the Qinghai-Tibet plateau. Journal of Wind Engineering and Industrial Aerodynamics 125, 30?37.

Cornelis, W., Gabriels, D., 2005. Optimal windbreak design for wind-erosion control. Journal of Arid Environments 61, 315–332.

Dong, Z., Luo, W., Qian, G., Wang, H., 2007. A wind tunnel simulation of the mean velocity fields behind upright porous fences. Agricultural and Forest Meteorology 146, 82–93.

Giannoulis, A., Stathopoulos, T., Briassoulis, D., Mistriotis, A., 2012. Wind loading on vertical panels with different permeabilities. Journal of Wind Engineering and Industrial Aerodynamics 107-108, 1–16.

Good, M.C., Joubert, P.N., 1968. The form drag of two-dimensional bluff-plates immersed in turbulent boundary layers. Journal of Fluid Mechanics 31(3), 547–582.

Guangyong, L., Peng, M., 2012. Wind-preventing sand-throwing wall - Patent number CN/102002916 B.

Hong, S.W., Lee, I.B., Seo, I.H., 2015. Modelling and predicting wind velocity patterns for windbreak fence design. Journal of Wind Engineering and Industrial Aerodynamics 142, 53–64.

Hotta, S., Horikawa, K., 1991. Function of sand fence placed in front of embankment, in: Coastal Engineering 1990, American Society of Civil Engineers, New York, NY. pp. 2754–2767.

Italferr, S., 2014. Preliminary design for Oman National Railway Project - segment 1 - Oman / UAE border at Al Buraimi - geotechnical study: Sand mitigation report.

Kerr, R.C., Nigra, J., 1952. Eolian sand control. Bulletin of the American Association of Petroleum Geologists 36, 1541–1573.

Letchford, C.W., Holmes, J.D., 1994. Wind loads on free-standing walls in turbulent boundary layers. Journal of Wind Engineering and Industrial Aerodynamics 51, 1–27.

Li, B., Sherman, D.J., 2015. Aerodynamics and morphodynamics of sand fences: A review. Aeolian Research 17, 33 – 48.

Lima, I.A., Araújo, A.D., Parteli, E.J., Andrade, J.S., Herrmann, H.J., 2017. Optimal array of sand fences. Scientific Reports 7 45148, 1–8.

Liu, B., Qu, J., Zhang, W., Qian, G., 2011. Numerical simulation of wind flow over transverse and pyramid dunes. Journal of Wind Engineering and Industrial Aerodynamics 99, 879 – 888.

Mendez, R., 2016. La arena invade tramos del ave a la meca ante la divisin del consorcio espaol. El Confidencial

Menter, F.R., 1994. Two-equation eddy-viscosity turbulence models for engineering applications. AIAA Journal 32, 1598–1605.

Menter, F.R., Kuntz, M., Langtry, R., 2003. Ten years of industrial experience with the sst turbulence model., in: Hanjalić, K., Nagano, Y., Tummers, J. (Eds.), Turbulence Heat and Mass Transfer 4: Proceedings of the Fourth International Symposium on Turbulence, Heat and Mass Transfer, Antalya, Turkey. Begell House Inc., Danbury, Connecticut.

Middleton, N., Sternberg, T., 2013. Climate hazards in drylands: A review. Earth-Science Reviews 126, 48 – 57.

Murakami, H., Sakamoto, H., 2001. Blowing-out snow protection fence having circular blade-type guide plate - Patent number JP/2001288715.

Pensa, M., Spirito Petrosino, P., Spirito Petrosino, G., 1990. Barriera Antivento, particolarmente per venti carichi di sabbia - Patent number IT/1224625.

Pettus Newell, J., 1903. Sand Guards for Railroad Tracks - Patent number US/731320.

Raffaele, L., Bruno, L., Pellery, F., Preziosi, L., 2016. Windblown sand saltation: a statistical approach to fluid threshold shear velocity. Aeolian Research 23, 79–91.

Redding, J., Lord, J., 1981. Designing for the effects of windblown sand along the new Jeddah-Riyadh-Dammam expressway, Proceedings of Symposium on Geotechnical Problems in Saudi Arabia, 363–396

Richards, P., Norris, S., 2011. Appropriate boundary conditions for computational wind engineering models revisited. Journal of Wind Engineering and Industrial Aerodynamics 99, 257–266.

Savage, R., Woodhouse, W., 1968. Creation and stabilization of coastal barrier dunes, in: Proceedings of the 11th Conference on Coastal Engineering Conference, London.

Schmidt, A., 2013. Santera 3000 technical sheet.

Stigter, C., Mohammed, A., Nasr Al-amin, N., Onyewotu, L., Oteng?id, S., Kainkwa, R., 2002. Agroforestry solutions to some african wind problems. Journal of Wind Engineering and Industrial Aerodynamics 90, 1101–1114.

Sweby, P.K., 1984. High resolution schemes using flux limiters for hyperbolic conservation laws. SIAM Journal of Numerical Analysis 21, 995–1011.

Zakeri, J., Forghani, M., 2012. Railway route design in desert areas. American Journal of Environmental Engineering 2, 13–18.

Zhang, C.L., Zou, X.Y., Cheng, H., Yang, S., Pan, X.H., Liu, Y.Z., Dong, G.R., 2007. Engineering measures to control windblown sand in Shiquanhe town, Tibet. Journal of Wind Engineering and Industrial Aerodynamics 95, 53 – 70.

Zhang, J., Cui, E., Fu, G., 1995. Investigation of the flow field and the starting conditions of wind-induced erosion of the railway embankment. Journal of Wind Engineering and Industrial Aerodynamics 54-55, 573–581.

Zhang, K., Qu, J., Liao, K., Niu, Q.H.and Ha, Q., 2010. Damage by wind-blown sand and its control along Qinghai-Tibet railway in China. Aeolian Research 1, 143–146.